INTERNATIONAL JOURNAL OF HYDROGEN ENERGY 46 (2021) 10666–10681

Available online at www.sciencedirect.com

ScienceDirect

journal homepage: www.elsevier.com/locate/he

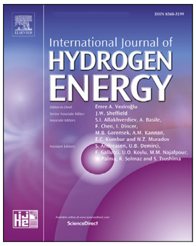

Dynamic system modeling of thermally-integrated concentrated PV-electrolysis

Isaac Holmes-Gentle, Saurabh Tembhurne, Clemens Suter, Sophia Haussener[*]

Laboratory of Renewable Energy Science and Engineering, EPFL, Station 9, Lausanne, 1015, Switzerland

HIGHLIGHTS

- A dynamic solar hydrogen processing plant model is developed and presented.
- Hysteresis observed in position of operating point in response to perturbations demonstrating a control challenge.
- The dynamic behavior is dependent on the operating point relative to the temperature stationary point.
- The opportunities for co-generation of hydrogen and heat from a thermally integrated system is found to be promising.

ARTICLE INFO

Article history:
Received 5 October 2020
Received in revised form
2 December 2020
Accepted 21 December 2020
Available online 6 February 2021

Keywords:
Solar fuels
Hydrogen production
Co-generation
Dynamic process modeling
Thermal integration

ABSTRACT

Understanding the dynamic response of a solar fuel processing system utilizing concentrated solar radiation and made of a thermally-integrated photovoltaic (PV) and water electrolyzer (EC) is important for the design, development and implementation of this technology. A detailed dynamic non-linear process model is introduced for the fundamental system components (*i.e.* PV, EC, pump *etc.*) in order to investigate the coupled system behavior and performance synergy notably arising from the thermal integration. The nominal hydrogen production power is ~2 kW at a hydrogen system efficiency of 16–21% considering a high performance triple junction III-V PV module and a proton exchange membrane EC. The device operating point relative to the maximum power point of the PV was shown to have a differing influence on the system performance when subject to temperature changes. The non-linear coupled behavior was characterised in response to step changes in water flowrate and solar irradiance and hysteresis of the current-voltage operating point was demonstrated. Whilst the system responds thermally to changes in operating conditions in the range of 0.5–2 min which leads to advantageously short start-up times, a number of control challenges are identified such as the impact of pump failure, electrical PV-EC disconnection, and the potentially damaging accentuated temperature rise at lower water flowrates. Finally, the simulation of co-generation of heat and hydrogen for various operating conditions demonstrates the significant potential for system efficiency enhancements and the required development of control strategies for demand matching is discussed.

---

[*] *Corresponding author.*
E-mail address: sophia.haussener@epfl.ch (S. Haussener).

https://doi.org/10.1016/j.ijhydene.2020.12.151

Introduction

One successful route to high efficiency solar-to-hydrogen conversion is the coupling of multi-junction photovoltaic (PV) cells to a water electrolyzer (EC) [1]. Whilst the current economic feasibility of solar hydrogen remains a topic of debate [2], costs of both the PV and EC components are reducing [3–6], and therefore it is a promising technology to realize the sustainable production of a critical chemical feedstock and potentially important energy carrier.

The thermal integration of the two energy conversion steps (*i.e.* solar energy to charge carriers, and charge carriers to chemical energy) has been shown to have a synergistic effect on the device performance, through both modeling [7–9] and experimental demonstration [8]. Here, we introduce a dynamic process model for a thermally and electrically integrated PV and electrolyzer (EC) operating under high solar concentrations. High optical concentration of solar radiation has the potential to be more economically competitive through the reduction in required photoabsorber material [10], however with the additional challenges associated with thermal management and higher current densities.

The main rationale for selecting a compact proton exchange membrane (PEM) EC for electrical and thermal coupling to the concentrated PV (CPV) is that external heat is often required for smaller stack sizes to maintain operating temperature [11]. Higher than ambient temperatures are advantageous as this reduces the irreversible energetic conversion losses in the EC by improving the kinetics and reducing membrane conductivity. Furthermore, PEM ECs have a fast response time and larger operational dynamic range, making this technology more suited to coupling with intermittent renewable power sources.

Fig. 1 shows the process flow diagram of our thermally integrated solar hydrogen processing system. Distilled water is pumped from the storage tank, through the deionizers and to the thermally integrated device consisting of a directly electrically connected PV module and an EC stack. Heat is then removed from the resulting oxygen-water stream with a heat exchanger before being transferred to a water-gas separator and subsequently compressed for storage. The hydrogen-water stream is passed directly to a water-gas separator before compression and storage. All water removed from the gas streams can then be recycled (only shown for the O_2 stream in Fig. 1 as this is the only stream that contains a significant flowrate of water).

In order to investigate the fundamental dynamics of the system, only key components (PV, EC, pump and piping) are selected from the complete generic system. This simplification means the dynamic behavior intrinsic to the proposed device can be studied whilst neglecting the extraneous downstream components, such as the liquid-gas separation and end user dependent gas processing steps. All the neglected components can be designed to meet the requirements imposed by the PV-EC dynamics studied herein. Furthermore, the power requirements of neglected components are not included and these include the energy requirements of gas drying and the biaxial solar tracking etc. Whilst these energy requirements may be significant and dependent on the

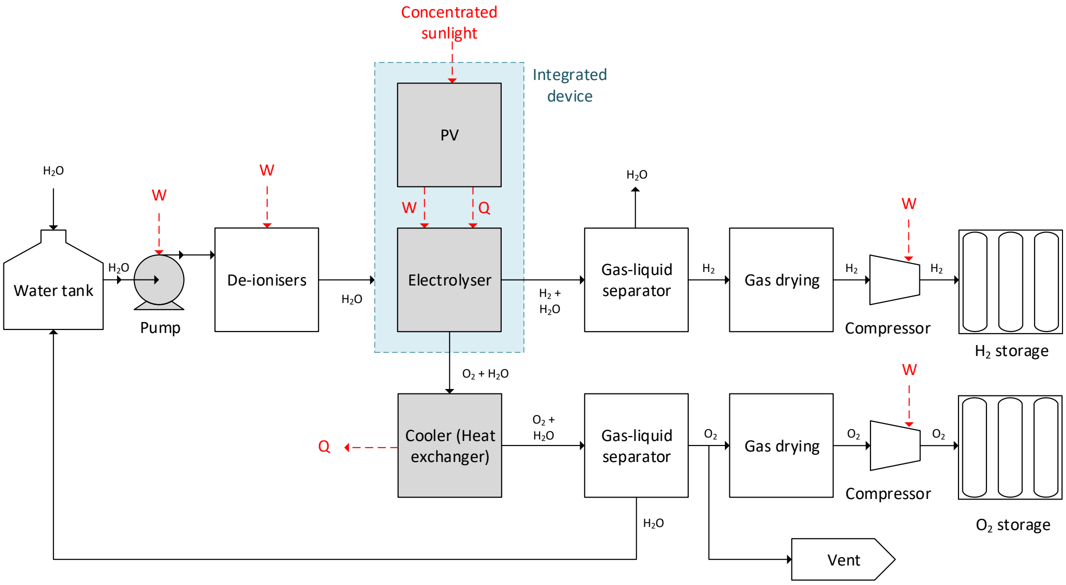

Fig. 1 – Process flow diagram for the generic solar fuel plant, converting concentrated solar energy to hydrogen and heat. Solid lines denote the transfer of material (fluid streams) where the annotation gives the constituent components (*e.g.* H_2O, H_2, O_2). Red dotted lines denote the energy transfer between unit processes where Q is heat and W is work. The components highlighted in grey are those modeled in this study. (For interpretation of the references to color in this figure legend, the reader is referred to the Web version of this article.)

configuration and fuel consumer, they will not affect the basis of this study: the fundamental dynamics of the thermally integrated PV-EC system.

Whilst simulation and optimisation of PV + EC with and without power conversion technologies is an established field [12–16], there have been relatively few studies looking at the synergistic thermal integration of PV-thermal and EC technologies [9,17]. Furthermore, the detailed dynamic behavior is often neglected on the basis of reducing model complexity for coupled PV-EC systems. As the system considered here is thermally integrated, the concentrated solar irradiance and operating conditions will significantly impact the operating temperatures, and hence it is expected to exhibit a dynamic response to a far greater extent than for non-concentrating PV fields coupled to power electronics and a temperature controlled EC. As comprehensively reviewed by Carmo et al. [18] there have been many time-dependent models of varying approaches developed for PEM ECs [19–24], but there have been no dynamic models of thermally coupled PV-EC using concentrated solar radiation. Whilst each component model is based directly on previous studies or the amalgamation of previous studies and heat transfer modeling, this model is original in its combination of components and integrated complexity. The dynamic behavior of the considered system: a thermally integrated and directly electrically coupled CPV + EC device has not yet been reported either theoretically or experimentally. Therefore, this model will facilitate new insight into the expected dynamic phenomena, highlight the synergistic effect of the integration and assess the impact on the system performance, and to discuss the consequences on the control strategy.

Model description

The modeled system is comprised of the following key components: 1) a high efficiency solar parabolic dish (estimated 86% mean optical efficiency), 2) a triple-junction (InGaP/InGaAs/Ge) concentrator solar module (30–36% solar-to-electricity efficiency at maximum power point), 3) a proton exchange membrane (PEM) EC (50–70% electricity-to-hydrogen efficiency based on Gibbs energy), and 4) auxiliary components such as a pump, piping and heat exchanger (HX) for heat recovery (assuming ideal effectiveness). The system was designed with a nominal hydrogen production power of approximately 2 kW under high solar irradiance (~1 kW m^{-2}).

PV module

Electrical model

A triple junction PV cell can be modeled as three single diode equivalent circuits (Eq. (1)) electrically coupled in series [25]. The current I_i and voltage V_i relation of a single junction subcell i of the triple junction requires knowledge of the reverse saturation current, $I_{o,i}$, series resistance, $R_{s,i}$, elementary charge, q, ideality factor, n_i, and Boltzmann constant k_B. It is assumed that the photo-current $I_{L,i}$ is equal to the short circuit current $I_{sc,i}$ and that the shunt resistance $R_{sh,i}$ is large. All junctions are assumed to be at the same temperature T_{PV}. Current matching of the subcell junctions are enforced by the equation: $I_1 = I_2 = I_3$.

$$I_i = I_{L,i} - I_{o,i}\left[\exp\left(\frac{q(V_i + I_i R_{s,i})}{n_i k_B T_{PV}}\right) - 1\right] - \frac{V_i + I_i R_{s,i}}{R_{sh,i}} \tag{1}$$

The short circuit current is assumed to be linearly proportional to the solar irradiance concentration, C [26]. C is a multiple of standard 1 Sun conditions where 1 Sun is equal to 0.9 kW m^{-2} (AM1.5D [27]). Temperature dependence of the short circuit current is approximated to be linear [28] within a defined temperature range where μ_{Isc} is a temperature dependent proportionality coefficient.

The diode reverse saturation current for junction i is a function of T_{PV}, bandgap $E_{g,i}$ and a number of constants κ_i, γ_i, n_i (Eq. (2)).

$$I_{o,i} = A_{PV,cell}\kappa_i T_{PV}^{(3+\gamma_i/2)}\exp\left(\frac{-E_{g,i}}{n_i k_B T_{PV}}\right) \tag{2}$$

The temperature dependence of the cell bandgap $E_{g,i}$ is commonly expressed as a function of T_{PV}, the bandgap at absolute zero E_g (0 K) and two material dependent properties α and σ as detailed by Varshni [29].

As the top two layers are semiconductor alloys, the bandgap can be approximated with a linear superposition of the properties of two constituent semiconductors (where x is the molar fraction of one of the semiconductors) and a correction factor f_{Eg} [30].

$$E_g(A_{1-x}B_x) = (1-x)E_g(A) + xE_g(B) - x(1-x)f_{Eg} \tag{3}$$

A PV module is composed of $N_{PV,s}$ number of triple junction equivalent circuit in series to make a single 'string' and $N_{PV,p}$ number of 'strings' in parallel. The PV module electrical potential $V_{PV} = N_{PV,s}V_{PV,\ cell}$ and current $I_{PV} = N_{PV,p}I_{PV,\ cell}$ are calculated accordingly. In order to reduce model complexity, it was assumed that all triple junction cells are identically performing and are homogeneously irradiated. However, it is important to note that this condition may not be met under a realistic solar flux distribution and should be studied further in future work. The PV module temperature T_{PV} is equal to the individual PV cells' temperature.

Thermal model

As high solar concentration ratios are considered in this work (>150), the CPV module will require active cooling [31]. The CPV module consists of 1) PV module comprised of various triple-junctions cells which are thermally bonded to a 2) copper heat sink which is cooled by 3) water. Therefore, a 0-dimensional thermal resistance model is employed where the PV module, the heat sink (HS) and the inlet/outlet cooling water (CW) are each defined by a temperature. This implies a homogeneous temperature distribution over the solar cells (*i.e.* input light is assumed uniform) and heat sink (justified by the high thermal conductivity of copper). The following three heat balances can be written as Eq. (4-6) where $H_{CW,inlet/outlet}$ is the inlet/outlet enthalpy of the cooling water, $P_{solar,PV}$ is the total solar input power to the module. f_{abs} is the fraction of light incident which is absorbed and the subscript "amb" denotes the ambient surroundings. Accumulation of heat is only considered in the heat sink, as it has a significant thermal mass C_{HS}.

$$0 = f_{abs} P_{solar,PV} - V_{PV} I_{PV} - Q_{PV \to HS} \tag{4}$$

$$C_{HS} \frac{dT_{HS}}{dt} = Q_{PV \to HS} - Q_{HS \to CW} - Q_{HS \to amb} \tag{5}$$

$$0 = H_{CW,inlet} - H_{CW,outlet} + Q_{HS \to CW} \tag{6}$$

Heat transfer between the PV and the heat sink is due to thermal conduction (Eq. (7)). $U_{PV \to HS}$ is the overall heat transfer coefficient and A_{PV} is the heat transfer area (*i.e.* the contacting area of the PV module). This heat transfer coefficient is considered constant over the temperature range and is calculated in the Supporting Information according to Theristis et al. [32].

$$Q_{PV \to HS} = U_{PV \to HS} A_{PV} (T_{PV} - T_{HS}) \tag{7}$$

The overall heat transfer coefficient for heat sink to ambient surroundings will be a function of wind speed, humidity *etc.* [33]. However, this dependence was neglected (*i.e.* $(UA)_{HS \to amb}$ assumed constant) given the dominance of the convective heat transfer to the cooling water.

$$Q_{HS \to amb} = (UA)_{HS \to amb} (T_{HS} - T_{amb}) \tag{8}$$

Forced convection through a micro-channeled heat sink is a proven method of cooling CPVs [31,34], and in this work we calculate the overall heat transfer coefficient and friction factor based on multiple thin channels on the backside of the heat sink.

This convective heat transfer is then expressed as Eq. (9) where the heat exchanger effectiveness ε for a heat exchangers with a single heat transfer fluid (*i.e.* a heater or cooler) is given by Eq. (10).

$$Q_{HS \to CW} = \varepsilon c_{p,CW} \dot{m}_{CW} (T_{HS} - T_{CW,inlet}) \tag{9}$$

$$\varepsilon = 1 - \exp(-NTU) \tag{10}$$

The Number of Transfer Units (NTU) is given by Eq. (11) where $c_{p,CW}$ is defined as the mean specific heat capacity at constant pressure over the temperature range and A_{HS} as the interfacial heat exchange surface area.

$$NTU = \frac{\eta_o U_{HS \to CW} A_{HS}}{c_{p,CW} \dot{m}_{CW}} \tag{11}$$

Assuming the overall heat transfer coefficient $U_{HS \to CW}$ is dominated by the interfacial convective transport, $U_{HS \to CW}$ can be calculated from Nusselt number correlations for fully developed laminar flow rectangular channels [35]. As detailed in the Supporting Information, an overall surface fin efficiency η_o is calculated assuming straight fins with an adiabatic tip to correct for the temperature distribution across the micro-channel fins [36]. Additionally, the energy balance over the cooling water is found in the Supporting Information.

Mass and momentum model

Within the operating conditions considered (<100 °C), water can be considered incompressible and therefore there is no mass accumulation of water within the CPV module. The pressure drop is given by the Darcy–Weisbach equation (Eq. (12)), where ρ is the fluid density and the friction factor f_D can be computed from empirical correlations for rectangular channels [35]. The mean velocity v within the channel of cross-sectional area $A_{HS,cross}$ and length L is calculated with $v = \dot{m}/\rho A_{HS,cross}$. D_h is the hydraulic diameter of the channel.

$$\Delta p = f_D \frac{L \rho v^2}{2 D_h} \tag{12}$$

PEM electrolyzer

Electrical model

The electrochemical performance of the PEM EC is coupled with a mass conservation model in order to simulate the dynamic behavior. The voltage *vs.* current dynamic response of a PEM EC is commonly assumed to be instantaneous [37] and therefore will be modeled with a time-invariant model. Consequently, any dynamics observed in the electrical variables will result from time-variant parameters (*e.g.* the species concentration, temperature, pressure *etc.*).

The overall chemical reaction in the EC is $H_2O \rightarrow H_2 + 1/2 O_2$ and for every molecule of hydrogen formed, two electrons must be transferred between the electrodes ($n_{e^-} = 2$). As this water splitting reaction is non-spontaneous ($\Delta G > 0$) in the temperature range considered, a negative cell potential is required to drive the reaction. For simplicity, we will express the cell potential as positive voltages. The EC's cell potential $V_{EC,cell}$ required to pass a given current can be written as the sum of the thermodynamic requirement, the redox potential E_{redox}, the electrochemical kinetics and the ohmic overpotentials. The concentration overpotential (due to mass transfer effects) is neglected as the typical current densities of commercial PEM ECs are sufficiently below the limiting current density [21,38].

The Nernst equation (Eq. (13)) relates the (reversible) electrochemical redox potential of water splitting E_{redox} to the standard electrode potential E_o for the operating conditions (T_{EC}, p_{H_2}, p_{O_2}, assuming the activity of water $a_{H_2O} = 1$). The temperature dependence of the standard electrode potential and the thermo-neutral potential are commonly expressed in the form of Eqs. (14) and (15), where the fitted parameters are calculated from thermophysical properties of water provided by NIST [39].

$$E_{redox} = E_o + \frac{RT_{EC}}{n_{e^-} F} \ln\left(\frac{p_{H_2} p_{O_2}^{1/2}}{a_{H2O}} \right) \tag{13}$$

$$E_o = 1.229 - 0.827 \times 10^{-3} (T_{EC} - 298) \tag{14}$$

$$E_{th} = 1.481 - 0.164 \times 10^{-3} (T_{EC} - 298) \tag{15}$$

The kinetic overpotential term is defined as the sum of the oxygen evolution reaction and hydrogen evolution reaction overpotentials, each of which can be related to the current *via* the Tafel equation. This simplification of the Butler-Volmer equation is valid as the normal operating range of PEM ECs means that low currents are inadvisable due to a resulting higher concentration of H_2 in the output O_2 stream.

$$\eta_{kinetic} = \frac{RT_{EC}}{\alpha_a n_e F} \ln\left(\frac{i_{EC,cell}}{i_{o,a}} \right) + \frac{RT_{EC}}{\alpha_c n_e F} \ln\left(\frac{i_{EC,cell}}{i_{o,c}} \right) \tag{16}$$

The temperature dependence of the anodic and cathodic exchange current density can be modeled using an Arrhenius type equation [7,21,40] where E_a is the activation energy and $i_{o,ref}$ is the exchange current density at a reference temperature T_{ref}.

The ohmic overpotential is given by the sum of the ohmic losses in the PEM (R_m) and in the external electrical circuit ($R_{external}$). The electrolytic resistance of the PEM (Eq. (17)) is a function of the membrane thickness δ_m, the geometric cell area $A_{EC,cell}$ and the membrane conductivity σ_m.

$$R_m = \frac{\delta_m}{A_{EC,cell}\sigma_m} \tag{17}$$

The membrane conductivity σ_m (in S cm^{-1}) can be calculated using the empirical correlation given in Eq. (18) as a function of temperature T_{EC} and the degree of humidification λ_m [41].

$$\sigma_m = (0.00514\lambda_m - 0.00326)\exp\left(1268\left(\frac{1}{303} - \frac{1}{T_{EC}}\right)\right) \tag{18}$$

Finally, the electrolyzer is comprised of $N_{EC,s}$ number of cells in series to make an electrolyzer stack. The stack potential $V_{EC} = N_{EC,s}V_{EC,cell}$ and the stack current $I_{EC} = A_{EC,cell}i_{EC,cell}$ are calculated accordingly.

Thermal model

The energy conservation in the electrolyzer is given in Eq. (19) where it is assumed the thermal mass C_{EC} is constant over the operational temperature range.

$$C_{EC}\frac{dT_{EC}}{dt} = Q_{gen} - Q_{loss} - Q_{fluid,a} - Q_{fluid,c} \tag{19}$$

The heat generated (or consumed) by the kinetic and ohmic losses of the reaction Q_{gen} is given by Eq. (20). The electrolyzer stack is considered to be well insulated and therefore the heat lost to the environment Q_{loss} is assumed to be zero. The heat transferred to the fluid in the anodic and cathodic chambers are given in Eq. (21) and Eq. (22), respectively. The driving temperature difference for heat transfer to the fluid is defined as the difference between the (uniform) cathode or anode chamber fluid temperature and the EC stack temperature.

$$Q_{gen} = A_{EC,cell}i_{EC,cell}N_{EC,s}(V_{EC,cell} - E_{th}) \tag{20}$$

$$Q_{fluid,a} = (UA)_{fluid,a}(T_{EC} - T_{fluid,out,a}) \tag{21}$$

$$Q_{fluid,c} = (UA)_{fluid,c}(T_{EC} - T_{fluid,out,c}) \tag{22}$$

Mass, energy and momentum model of fluid streams

The mass and energy conservation model was applied to the anodic and cathodic chamber separately. For all components i, a component mass balance can be specified in Eq. (23) where M_i, $x_{inlet/outlet,i}$, $\dot{m}_{inlet/outlet}$, $M_{w,i}$ and υ_i are the accumulated mass of i, mass fraction of i, total mass flowrate, molecular weight of i, stoichiometry coefficient of component i, respectively. R_{rxn} is the molar reaction rate and is calculated using Faraday's law of electrolysis: $R_{rxn} = (\eta_F I_{EC} N_{EC,s})/(n_e F)$.

$$\frac{dM_i}{dt} = x_{inlet,i}\dot{m}_{inlet} - x_{outlet,i}\dot{m}_{outlet} + M_{w,i}\upsilon_i R_{rxn} \tag{23}$$

Assuming ideal mixing, the total anodic or cathodic chamber volume is the sum of the component volumes (Eq. (24)). It was assumed a negligibly small fraction of the chamber is compressible (following ideal gas law) which circumvented the need for two separate models for incompressible and compressible flow to account for gas production discontinuities (*e.g.* during start-up or shut-down). This fraction was set to be 0.1% of the total chamber volume at ambient conditions as compromise between model robustness and accuracy. The ideal component volumes are calculated using $V_i = M_i/\rho_i$ where the density is a function of chamber pressure and temperature.

$$V_{total} = \sum_i (V_i) + V_{compressible} \tag{24}$$

The energy balance over the EC chamber is given in Eq. (25). The energy accumulated E_{holdup} can be related to the state variable of the accumulated mass through Eq. (26) where the specific enthalpy in the chamber is calculated through an empirical correlation (*e.g.* $h = f(T, P, x)$).

$$\frac{dE_{holdup}}{dt} = h_{inlet}\dot{m}_{inlet} - h_{outlet}\dot{m}_{outlet} + Q_{fluid} \tag{25}$$

$$E_{holdup} = M_{total}h - PV_{total} \tag{26}$$

The gas crossover through the membrane has been identified as a problem in PEM ECs [42] and impacts the operational range of PEM ECs. Whilst this mass transport across the membrane is neglected in this study, the typical operational range of PEM ECs (10–100% of nominal power [18]) imposed by this phenomenon is considered.

The pressure drop over the anodic chamber of the EC is complex to model from first principles due to the two phase flow during gas production, entrance effects and complex geometry of flow plate. Therefore computational fluid dynamics is typically employed. We used a phenomenological model to obtain an order of magnitude pressure drop shown in Eq. (27) where Q_L is the liquid volumetric flowrate, K_{flow} is an empirical flow coefficient and a_{flow} is flow exponent determined by the flow regime (*i.e.* laminar, turbulent). This model assumes that the fluid passes through the $N_{EC,s}$ number of cells in parallel, the flow is laminar in the channels ($a_{flow} = 1$ [43]) and that the pressure drop is independent of the gas production rate. Furthermore, the pressure drop in the cathodic chamber is neglected.

$$\Delta p = K_{flow}\left(\frac{Q_L}{N_{EC,s}}\right)^{a_{flow}} \tag{27}$$

Auxiliary components

Solar dish

The solar parabolic dish receives the Direct Normal Irradiance (DNI) and reflects this towards the CPV module. The total amount of solar power transferred to the CPV, $Q_{solar\rightarrow CPV}$, is calculated by Eq. (28), where A_{dish} is the area of light collected by the dish. The optical efficiency η_{opt} can be decomposed into the multiplication of the solar weighted reflectance ρ_s, the intercept factor γ_{dish} and a dish cleanliness factor η_{clean} (typically between 0.7 and 1 [44]).

$$Q_{solar\rightarrow CPV} = \overbrace{\rho_s \gamma_{dish} \eta_{clean}}^{\eta_{opt}} A_{dish} \times DNI \tag{28}$$

Pump

Pumping power can be calculated from Eq. (29), where η_{pump} is the pump efficiency and is assumed constant. F_{pump} is the volumetric flowrate and Δp_{sys} is the total pressure drop over the system (*i.e.* piping, PV and EC).

$$P_{pump} = \frac{\Delta p_{sys} F_{pump}}{\eta_{pump}} \tag{29}$$

Piping

The gPROMS process model library pipe component [45] was used where the Haaland equation (Eq. (30)) calculates the turbulent flow Darcy friction factor f_D from the roughness ε_{pipe} and internal diameter d_{pipe}. The pressure drop is then calculated using the Darcy–Weisbach equation (Eq. (12)).

$$\frac{1}{\sqrt{f_D}} = -1.8\log\left[\left(\frac{\varepsilon_{pipe}/d_{pipe}}{3.7}\right)^{1.11} + \frac{6.9}{Re}\right] \tag{30}$$

Efficiency definitions

The overall system solar-to-hydrogen efficiency is defined by Eq. (31) using the Gibbs free energy of water electrolysis (ΔG_{rxn} = 237.1 J mol^{-1}). The thermal system efficiency is defined by Eq. (32) where Q_{HX} is the useful thermal power extracted from the heat exchanger (HX). The total input solar power P_{solar} is defined based on the DNI ($P_{solar} = DNI \times \pi D_{dish}^2/4$). In this work, only the pumping power P_{pump} is considered (*i.e.* $P_{other} = 0$). The system efficiency of co-generation of heat and fuel is then defined as $\eta_{sys} = \eta_{H_2} + \eta_{thermal}$.

$$\eta_{H_2} = \frac{R_{rxn}\Delta G_{rxn}}{P_{solar} + P_{pump} + P_{other}} \tag{31}$$

$$\eta_{thermal} = \frac{Q_{HX}}{P_{solar} + P_{pump} + P_{other}} \tag{32}$$

The component electrical efficiencies for the PV module and the PEM stack (based on ΔG_{rxn}) are defined as Eq. (33), where $P_{solar,PV}$ is the total power of solar radiation incidence on the PV cells. Here, V_{PV}^{mpp} and I_{PV}^{mpp} are the voltage and current at the Maximum Power Point (MPP).

$$\eta_{PV}^{mpp} = \frac{V_{PV}^{mpp} I_{PV}^{mpp}}{P_{solar,PV}} \qquad \eta_{EC} = \frac{\eta_F E_{redox}}{V_{EC,cell}} \tag{33}$$

Solution of numerical model

The numerical solution of the mixed differential-algebraic model was accomplished with gPROMS ModelBuilder 5.1.1. The standard solver (DAEBDF) based on Backward Differentiation Formulas was used. The inbuilt PhysProp package was used for all thermodynamic calculations not explicitly specified in the following section.

Parameters and input datasets

This model is based on a dataset taken from literature, manufacturer datasheets and estimated from typical values or empirical correlations. The key parameters are given in Table 1, highlighting which parameters are design decisions. The nominal hydrogen production power of the designed system is approximately ~2 kW (based on enthalpy) for a DNI = 1000 W m^{-2} which corresponds to an input solar power of ~8.5 kW.

PV module

A summary of the key parameters and data sources used in the PV model is given in Table 1. For readability, all the triple junction PV electrical performance parameters are referenced as Ref. [25] and in turn are taken from a range of sources [30,61–65]. Other electrical (*e.g.* $N_{PV,s}$, $N_{PV,p}$, $A_{PV,cell}$) and thermal (*e.g.* C_{HS}, D_h, A_{cross}, A_{surf} *etc.*) properties were approximated based upon the Azur ADAM module [46]. In the absence of pressure drop data or heat transfer coefficients, it was assumed that there are 100 channels of dimensions 5.5 × 1 × 120 mm separated by copper fins of thickness 0.2 mm as this geometry leads to reasonable values for Nu_{D_h} & $f_D Re_{D_h}$ (following Ref. [35,36]) from which $U_{HS\rightarrow CW}$ can be calculated. $U_{PV\rightarrow HS}$ was calculated based on the thermal conductivity of the various constituent layers of the PV module (InGaP/InGaAs/Ge PV cell, copper, Al_2O_3) assuming the thermal conductivity of the triple junction is that of the thickest component, Ge [32]. Correlations for the thermodynamic proprieties for water were taken from literature (k [66], μ [67], c_p [68]). Whilst the critical maximum cell temperature specification varies between manufacturers, 100 °C is a commonly stated value [32] and will be considered in this work.

Electrolyzer stack

A Giner ELX Pemi 16 cell stack (50 cm^2 active nominal cell area) was used as a guideline for the ascertainment of the EC model parameters. As there is a wide range of exchange current density reported in literature [18], particularly for the oxidation reaction (10^{-13} to 10^{-3} [22,69,70]), the model was validated against experimental data. Values for $i_{o,a,ref}$, $i_{o,c,ref}$, λ_m, $R_{external}$ were determined using nonlinear least-squares data fitting. The reference temperature in the equation for the temperature dependence of exchange current density (see Supporting Information) is specified as 353.15 K and all the remaining estimated parameters were taken from literature or the EC datasheet. The fitted value for the degree of humidification λ_m (=18.2) was found to be within the expected range of 11–22 [71]. The key thermal property $(UA)_{fluid,a}$ was estimated from a numerical study [38], using the inlet and outlet fluid temperatures, fluid flowrate and mean stack temperature. Realistic estimates for $(UA)_{fluid,a}$, $(UA)_{fluid,c}$, $V_{a,total}$, $V_{c,total}$, C_{EC} are given in Table 1.

Table 1 — Overview of key model parameters. Junction 1, 2 and 3 of the triple junction PV cell are abbreviated as j1, j2, and j3, respectively. The sources of the parameters is listed with the following superscript nomenclature:^{1} Design decision,^{2} Estimate,^{3} Directly taken from,^{4} Typical value based on.

Symbol	Description	Value	Unit	Source
PV cell and module model:				
$N_{PV,s}$	Number of triple junction PV cells in series in a single 'string'	24	–	^{1}
$N_{PV,p}$	Number strings in parallel to make a PV module	4	–	^{1}
$A_{PV,cell}$	Area of single cell	1.04	cm^2	[46]^2
κ_1, κ_2, κ_3	Material constants (j1, j2, j3)	1.833×10^{-4}, 2.195×10^{-3}, 19.187×10^{-2}	$A\ m^{-2}\ K^{-4}$	[25]^3
n_1, n_2, n_3	Diode ideality factor (j1, j2, j3)	1.89, 1.59, 1.43	–	[25]^3
γ_1, γ_2, γ_3	Material constants (j1, j2, j3)	1.81, 1.86, 1.44	–	[25]^3
R_s	Total series resistance of all junctions	0.023	Ω	[25]^3
$i^{\circ}_{sc,1}$, $i^{\circ}_{sc,2}$, $i^{\circ}_{sc,3}$	Short circuit current density at 298.15 K (j1, j2, j3)	126, 127, 190	$A\ m^{-2}$	[25]^3
$\mu_{Isc,1}$, $\mu_{Isc,2}$, $\mu_{Isc,3}$	Temperature dependence coefficient for I_{sc} (j1, j2, j3)	6.3×10^{-4}, 6.3×10^{-4}, 3.6×10^{-4}	K^{-1}	[25]^2
$f_{Eg,1}$, $f_{Eg,2}$	Bandgap correction factor for j1 & j2	1.018, 1.192	eV	[25]^3
$E^{\circ}_{g,GaP}$, $E^{\circ}_{g,InP}$, $E^{\circ}_{g,GaAs}$, $E^{\circ}_{g,InAs}$, $E^{\circ}_{g,Ge}$	Bandgap of GaP, InP, GaAs, InAs, Ge at 0 K	2.857, 1.411, 1.519, 0.42, 0.7437	eV	[25]^3
α_{GaP}, α_{InP}, α_{GaAs}, α_{InAs}, α_{Ge}	Material constant for GaP, InP, GaAs, InAs, Ge	5.771×10^{-4}, 3.63×10^{-4}, 5.405×10^{-4}, 4.19×10^{-4}, 4.774×10^{-4}	$eV\ K^{-1}$	[25]^3
σ_{GaP}, σ_{InP}, σ_{GaAs}, σ_{InAs}, σ_{Ge}	Constant for GaP, InP, GaAs, InAs, Ge	372, 162, 204, 271, 235	K	[25]^3
$U_{PV \rightarrow HS}$	Heat transfer coefficient PV to heat sink	40	$kW\ m^{-2}\ K^{-1}$	^{2}
f_{abs}	Fraction of light absorbed by PV	0.95	–	[47–49]^4
C_{HS}	Thermal mass	700	JK^{-1}	[46]^2
D_h	Hydraulic diameter of channels	1.7	mm	[46]^2
A_{cross}	Cross-sectional area of cooling channels	5.4	cm^2	[46]^2
A_{surf}	Total heat transfer surface area of cooling channels	1600	cm^2	[46]^2
Nu_{D_h}	Nusselt number (based on the hydraulic diameter)	5.3	–	[35]^2
$f_D Re_{D_h}$	Darcy friction factor × Reynolds number	78.0	–	[35]^2
$(UA)_{HS \rightarrow amb}$	Heat transfer coefficient HS to ambient × area	10	WK^{-1}	^{2}
Electrolyzer cell and stack model:				
$N_{EC,s}$	Number of cells in series	32	–	^{1}
$A_{surf,cell}$	Surface area of a single cell	50	cm^2	[50]^3
η_F	Faradaic efficiency	1	–	^{2}
α_a, α_c	Charge transfer coefficient	0.5, 0.5	–	[51]^4
E_a	Anodic activation energy	40	$kJ\ mol^{-1}$	[52–55]^4
E_c	Cathodic activation energy	20	$kJ\ mol^{-1}$	[56, 51]^4
δ_m	Membrane thickness	100	μm	[57]^2
$R_{external}$	External ohmic cell resistance	8.54×10^{-4}	Ω	[50]^2
$i_{o,a,ref}$, $i_{o,c,ref}$	Anodic & cathodic exchange current density at 353.15 K	5.93×10^{-3}, 1.00×10^{-1}	$A\ cm^{-2}$	[50]^2
λ_m	Degree of membrane humidification	18.2	–	[50]^2
$V_{a,total}$, $V_{c,total}$	Anodic & cathodic chamber volume	800, 800	cm^3	^{2}
C_{EC}	Thermal mass	1000	JK^{-1}	^{2}
$(UA)_{fluid,a}$	Heat transfer coefficient to anodic chamber fluid	$25 \times N_{EC,s}$	WK^{-1}	[38]^2
$(UA)_{fluid,c}$	Heat transfer coefficient to cathodic chamber fluid	$10 \times N_{EC,s}$	WK^{-1}	^{2}
Solar dish model:				
D_{dish}	Dish diameter	3.3	m	^{1}
ρ_s	Solar weighted reflectance	0.90	–	[58]^4
γ_{dish}	Intercept factor	0.95	–	[59]^4
Pump and piping models:				
η_{pump}	Pump efficiency	0.7	–	[60]^4
L_{pipe}	Pipe length	10	m	^{2}
d_{pipe}	Pipe inside diameter	0.01	m	^{2}
ε_{pipe}	Pipe roughness	1.5	μm	^{2}

Auxiliary components

The solar dish diameter was specified as 3.3 m so that at DNI = 1000 W m^{-2}, 7.3 kW of power is delivered to the CPV corresponding to a solar flux concentration ratio of 732.5 or C = 813.8 suns (according to the definition of AM1.5D). The parabolic dish was assumed to be clean ($\eta_{clean} = 1$), of high optical performance and made of an aluminum based reflector (see Table 1).

Irradiance data and environmental conditions

The typical range of the Direct Normal Irradiance (DNI) was used based on experimental data collected at EPFL Lausanne (SPN1 Sunshine Pyranometer). The DNI was varied between 500 and 1000 W m^{-2} to represent differing meteorological conditions. The ambient temperature was assumed to be constant: $T_{amb} = 20$ °C.

Results and discussion

Steady-state sensitivity analysis

The position of the operating point of the integrated PV-EC device is heavily dependent on the operating temperature of both devices. In order to investigate this effect, only the PV and EC electrical models were solved assuming $T_{PV} = T_{EC}$ as a first assumption. Fig. 2a shows the PV and EC current-voltage curves highlighting the operating point for various T_{PV}, C, and $N_{EC,s}$. In a similar manner to García-Valverde et al. [12], the ratio of the number of EC cells to PV cells could be used as an optimisation parameter for the coupling efficiency, that is maximising the power transferred with respect to the maximum power of the PV. For all cases simulated, the increase in temperature reduces the operating voltage. For the operating current, two contrasting behavior are observed dependent on the relative position of the operating point to the Temperature Stationary Point (TSP) of the PV curve. We define the TSP as the point where $\frac{dI_{PV}}{dT_{PV}} = 0$ and is shown in Fig. 2b where the TSP is found at lower voltages/higher currents than the maximum power point (MPP). For operating voltages (V_{op}) lower than TSP voltage (V_{TSP}), the current increases moderately as the short circuit current increases with temperature. Conversely, for $V_{op} > V_{TSP}$ the current decreases significantly as the open circuit voltage decreases. This crude analysis ($T_{PV} = T_{EC}$) succinctly demonstrates the necessity for an accurate thermal model due to the sensitivity of the system performance to temperature.

Following this, the complete dynamic model was solved in order to determine the PV and EC steady state temperatures for various conditions through simulation over adequately long timescales (*i.e.* ~1000s of seconds). As expected, the operating temperatures increase with decreasing flowrate and at lower flowrates (<2 L min^{-1}) a stronger rise in temperature is observed (see in Fig. 3b for DNI = 1000 W m^{-2}). This strong increase in temperature potentially poses a control challenge which will be subsequently explored, as a small perturbation in flowrate could lead to a large rise in operating temperature. Furthermore, Fig. 3b shows that the temperature difference between PV and EC is also a function of water flowrate (*i.e.* difference increasing with increasing flow rate), due to the changing effectiveness of the heat transfer to the water in the PV heat sink.

For F_{pump} varying between 1 and 10 L min^{-1} and $N_{EC,s}$ between 28 and 40 (see Fig. 3a), the maximum efficiency is in the range of ~16–21% and significantly contrasting behavior at different coupling ratios (*i.e.* $N_{EC,s}/N_{PV,s}$) is observed. For smaller $N_{EC,s}$ (*e.g.* $N_{EC,s} = 28, 30, 32$), the maximum efficiency is obtained at the lowest permissible flowrates and therefore highest operating temperatures. For higher coupling ratios (*e.g.* $N_{EC,s} = 34, 36, 38, 40$) when the operating point is at higher voltages than the maximum power point of the PV, the

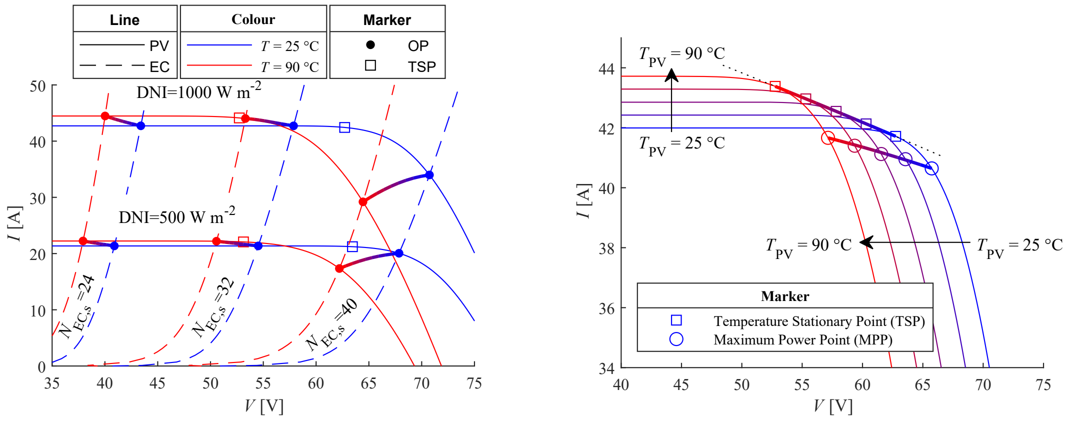

(a) (b)

Fig. 2 – a) Steady-state electrical model (PV, EC) for two hypothetically equal operating temperatures denoted as $T = T_{EC} = T_{PV}$ highlighting the position of the temperature stationary point (TSP). The continuum of operating points (OP) at intermediate temperatures is displayed as a line with linear color gradient. b) The current-voltage relationship of the PV module highlighting the position of the maximum power point (MPP) and the temperature stationary point (TSP) is shown for T_{PV} between 25 and 90 °C. (For interpretation of the references to color in this figure legend, the reader is referred to the Web version of this article.)

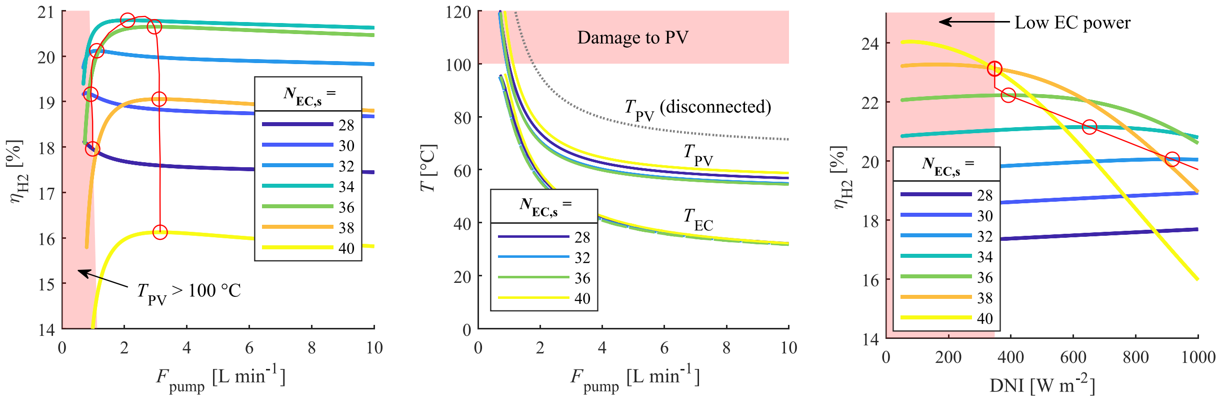

(a) (b) (c)

Fig. 3 – a) Hydrogen system efficiency *vs.* water flowrate for various $N_{EC,s}$. b) The steady-state system temperatures (PV and EC) *vs.* water flowrate for various $N_{EC,s}$. Additionally, the steady-state PV temperature resulting from electrical disconnection is shown and is not dependent on $N_{EC,s}$. c) Hydrogen efficiency *vs.* DNI for various $N_{EC,s}$ where water flowrate = 2 L min^{-1}. In both a)&c) the red line denotes the respective operating conditions which maximize the efficiency for each $N_{EC,s}$ within operational limits (*i.e.* T_{PV} < 100°C and I_{EC} > 15 A [50]). (For interpretation of the references to color in this figure legend, the reader is referred to the Web version of this article.)

highest efficiencies are conversely found at higher flowrates and therefore lower T_{PV}. This behavior can be explained by the previous discussion of Fig. 2a, where the effect of the increase in short circuit current dominates over the decrease in open circuit voltage for lower coupling ratios and *vice-versa* for higher coupling ratios. For larger flow rates (5–10 L min^{-1}), a decrease in efficiency is again observed, resulting from the increase in the pumping power adversely affecting the efficiency.

Additionally, Fig. 3a shows that there is a significant decrease in η_{H_2} at higher coupling ratios for water flowrates <2 L min^{-1}. This leads to a larger fraction of solar irradiance that is converted to heat and the significant resistance to heat transfer leads to an increase in PV temperature, which can further shift the operating point. This positive feedback loop accentuates the control challenge at flowrates <2 L min^{-1} and conceptually could lead to thermal runaway type situation which is investigated further in the following discussion.

The sensitivity of the fuel conversion efficiency to the DNI is shown in Fig. 3c and the observed behavior can be explained by to the logarithmic dependence of the open circuit voltage and linear dependence of the short circuit current with light intensity (which shifts the maximum power point voltage) while also considering a temperature effect (as the operating temperatures are dependent on irradiance). This, in turn, affects the voltage–current coupling of the PV and EC which impacts the system efficiency accordingly (dependent on the operating point relative to the TSP). As DNI increases, the TSP shifts to lower potentials while the operating voltage moves to larger potentials (as current increases) whilst also considering the increased operating temperatures which reduces the TSP significantly and the operating point to a lesser extent. The resulting general behavior is that increasing DNI leads to a better coupling efficiency when $V_{op} < V_{TSP}$ (see $N_{EC,s}$ = 28 in Fig. 3c) up until $V_{op} > V_{TSP}$ where an increasing DNI leads to a worse coupling efficiency (see $N_{EC,s}$ = 40 in Fig. 3c).

System dynamics

Response to step changes

The system behaves dynamically due to the differential terms in the energy and mass balances with accumulation terms (Eq. (5), (19), (23) and (25)). The observed dynamic electrical performance of the CPV and the EC originates from the changes in their operating temperatures and pressures as both electrical models respond instantaneously. We considered the major disturbance to be DNI and major controlled variable to be the water flowrate. Various instantaneous step changes in DNI and F_{pump} are made in order to investigate the system dynamics.

Firstly, the system response to a step change in water pump flowrate at constant DNI was investigated. Fig. 4 demonstrates the system's non-linear behavior. The response curve of the PV temperature is approximately first order where the time constant depends on the water mass flowrate $\dot{m}_{CW}$. This dependence can be seen in the dynamics of the heat sink temperature T_{HS} when expressed in a first order time constant form by rearranging Eqs. (4), (5), (8) and (9): $\tau \frac{dT_{HS}}{dt} + T_{HS} = f(t)$ where $\tau = \frac{C_{HS}}{\varepsilon c_{p,CW}\dot{m}_{CW} + (UA)_{HS}}$. Then, $T_{PV} = f$ (T_{HS}, $P_{solar,PV}$, V_{PV}, I_{PV} ...) as given by Eqs. (7) and (4) and for minor changes in operation point (*i.e.* $V_{PV}I_{PV}$ ~ constant) $T_{PV} \propto T_{HS}$. This explains the hysteresis observed between positive and negative steps in F_{pump}, as negative steps end on differing values of F_{pump} (1, 2 L min^{-1}) whereas positive steps end on F_{pump} = 3 L min^{-1}.

The EC temperature follows a similar trends as discussed for T_{PV} with the addition of damped second order dynamics observable in the first couple of seconds where the rate of temperature rise is delayed. The differences in the dynamics of T_{EC} when DNI = 500 and 1000 W m^{-2} are due to the fact energy must first accumulate in the EC anodic chamber before the temperature gradient between EC and anodic chamber

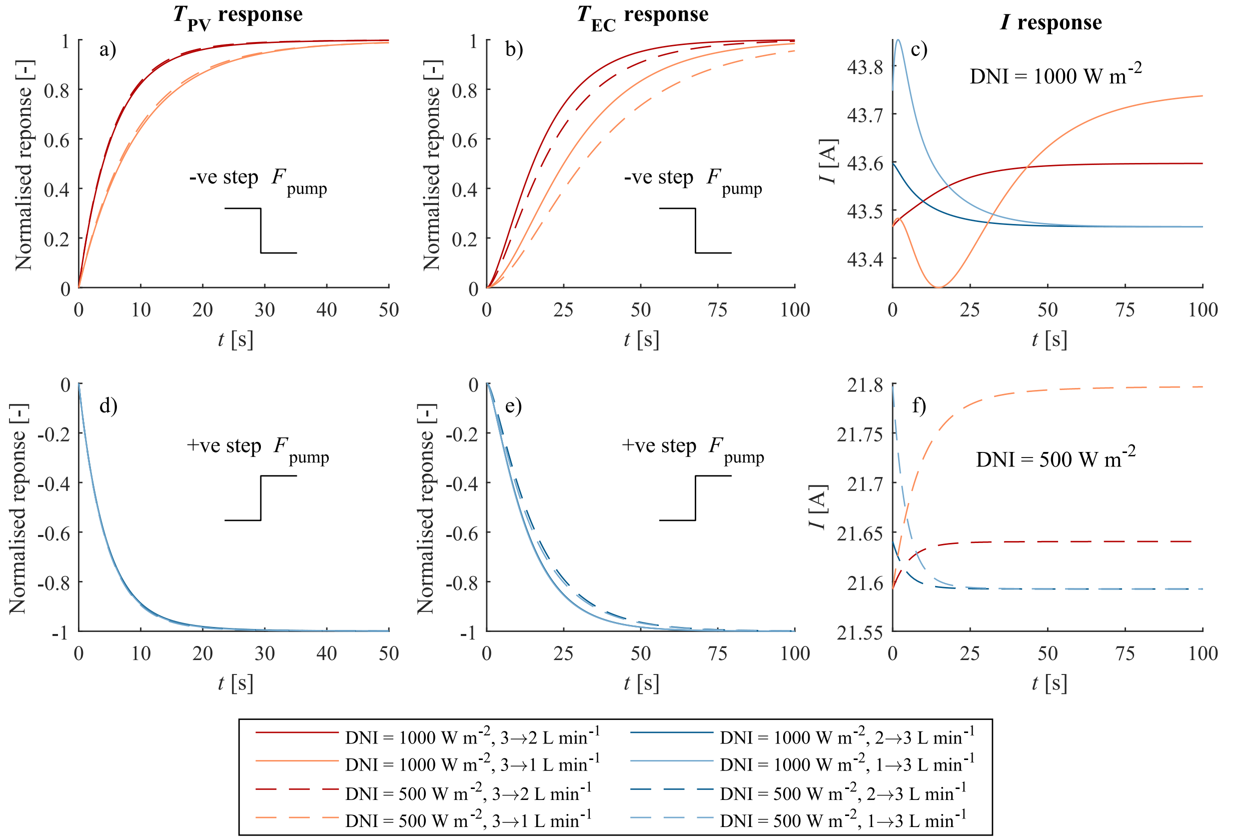

Fig. 4 – System response to step changes in F_{pump} and DNI with $N_{EC,s} = 32$, both for various step sizes. a) & d) show the normalized T_{PV} response and b) & e) show the normalized T_{EC} response. Negative step changes are shown in a) & b) whereas positive step changes are shown in d) & e). The normalized temperature response is defined as $(T(t) - T(t = \infty))/(T(t = 0) - T(t = \infty))$. c) and f) show the current response for DNI = 1000 W m^{-2} and DNI = 500 W m^{-2}, respectively.

temperature rises and is therefore dependent on the inlet enthalpy (which is dependent on DNI).

The response time of T_{PV} is about 2–3 times as fast compared to T_{EC} (see Fig. 4). The response at DNI = 1000 W m^{-2} and a step change in F_{pump} from 3 to 1 L min^{-1} (orange unbroken line in Fig. 4) is particularly notable as multiple phenomena are observed. Initially, $V_{op} < V_{TSP}$ and when the PV temperature rises faster than the EC temperature the short circuit current increase leads to a small increase in current (0–1.7 s) before the increase in T_{PV} leads to the operating point crossing the TSP ($V_{op} > V_{TSP}$) and the reduction in open circuit voltage dominating the electrical performance causing a reduction in current (1.7–14 s). Next, as the temperature of EC starts rising, the reduction in EC overpotentials dominates leading to the current ultimately rising to the steady-state value (14+ sec).

Following this, the trajectory of the operating point (in the current-voltage domain) as a function of time for step changes in F_{pump} and DNI is investigated for varying $N_{EC,s}$. Fig. 5 demonstrates the hysteresis in operating point trajectory due to the contrasting time scales between the temperature response of the PV and the EC (specifically, the PV temperature responds faster). Additionally, Fig. 5 shows a PV temperature overshoot for $N_{EC,s} = 40$ as the position of the electrical coupling (*i.e.* right of MPP) makes it particularly sensitive to temperature changes. Shown in Fig. 5c for the step decrease in F_{pump}, the operating current passes through a minimum before increasing to the steady-state value caused by the delayed temperature increase in T_{EC}. As the electric power extracted increases, the PV heat transfer requirements decrease leading to the ultimately lower T_{PV}. This demonstrates the highly coupled nature of operating conditions, temperatures, and power. Correspondingly, the system response to step changes in DNI can be seen in Fig. 6 where the initial instantaneous change in operating point is caused by the dependence of the PV short circuit current on the solar concentration and which is then followed by a response comparable to Fig. 5 caused by the thermal dynamics.

This analysis shows that dynamic effects are observed, specifically operating temperatures stabilize within 1–2 min for changes in DNI and water flowrate, which is comparable to the timescales of typical intermittent irradiance conditions. This highlights the control challenge of stable operation under cloudy conditions. However, the system is very responsive to changes in DNI, as seen in Fig. 6 indicating that intermittent conditions will not cause a significant reduction in H_2 efficiency. It is important to note that in this work a comparatively small electrolyzer (nominal power ~3 kW) was modeled and a larger system would have slower thermal dynamics due to the higher thermal inertia of the components. This could potentially represent a greater control challenge but the close coupling of the EC and the solar dish CPV system limits the size of the EC stack due to constraints in the feasible solar parabolic dish areas and the diffuse nature of solar irradiance.

Pump failure and electrical disconnection

Of particular importance for the development of a suitable operating procedure is how the system responds to major deviation to normal operation such as water pump failure or the electrical disconnection of the PV to the EC.

Pump failure leads to a surface temperature of the PV greater than 100 °C within seconds at an approximately linear rate of ~6 K s^{-1} when PV and EC are electrically coupled for DNI = 1000 W m^{-2}. If the electrical power is not transferred from the PV (*i.e.* disconnected) the rate is greater at ~9 K s^{-1}. The ramification of this is that high frequency monitoring of the water flowrate and responsive control is mandatory to ensure that the pump failure is detected quickly (<1 s) and the reactor is moved out of focus (~1 − 3 s) or protected by a shield.

As all light absorbed by the PV module that is not removed as work, will be converted to heat, electrical disconnection of the PV to the EC may also lead to unacceptably high PV temperatures, particularly for lower water flowrates. This disconnection could occur due to failure of an electrical connection/switch or accidental operator error. As shown in Fig. 3b, the increase in disconnected PV temperature with decreasing F_{pump} follows the same trend as when PV-EC are connected but at a larger magnitude. *I.e.* T_{PV} when disconnected at F_{pump} =2 L min^{-1} is 96 °C (compared to $T_{PV} = 71$ °C for the connected case for $N_{EC,s} = 32$), and passes an unsupportable 100 °C at $F_{pump} = 1.8$ L min^{-1}. Analogous to the issue of pump failure, electrical disconnection will also require monitoring and response (*i.e.* the dish moved out of focus and maximum water flowrate applied) within comparably fast time scales (<3 s).

Assessing feasibility of thermal runaway

In the steady-state analysis, it was shown that a reduction in PV electrical power causes an increase in the heat required to be dissipated which leads to increased T_{PV}. It was speculated that a thermal runaway situation could occur when the operating point voltage was higher than the TSP voltage, as an increase in temperature could reduce the open circuit voltage and the intersection point of the PV and EC curves would reduce the electrical power of the PV, which further increases the PV temperature and thereby creating a feedback loop.

In order to investigate the stability of this temperature accentuating effect, Fig. 7 was constructed in a manner equivalent to a Semenov diagram, which is typically used in the stability analysis of thermal runaway scenarios. The theoretical amount of heat generated in the PV *versus* the theoretical amount of heat removed was plotted for different PV temperatures (assuming all other temperatures remain at the steady-state operating point).

This analysis shows that for all intersecting points (which can represent a stable or unstable steady-state solution) in Fig. 7, the gradient of Q_{out} at a given T_{PV} is larger than the gradient of Q_{in}, indicating a stable equilibrium state. Essentially, an infinitely small perturbation in T_{PV} will lead to more heat being dissipated than generated and so the operating point will return to the stable solution. Given the form of the equations and that the maximum amount of heat into the system corresponds to the total solar input (*i.e.* no electrical power extracted), there will be no unstable solutions (as the gradient of Q_{in} cannot be greater than Q_{out}). This analysis assumes that a diode is used to prevent reverse current flow so that the EC cannot operate in reverse (*i.e.* fuel cell mode). In a diode-less scenario, unstable thermal runaway may be possible as the maximum amount of heat in is no longer constrained to P_{solar} and will include the electrical power from reverse operation dissipated as heat in the PV. This is only anticipated to happen at impermissibly high T_{PV} as a significant change in the open circuit voltage and respective operating point is required to obtain a significant reverse current. Regardless, prevention of any reverse current using a diode is highly recommended.

Therefore, whilst this analysis has demonstrated that this phenomenon is stable (T_{PV} will remain bounded), the reduction in power does significantly increase the heat dissipation requirements for larger values of $N_{EC,s}$ (*cf.* gradient of Q_{in} for $N_{EC,s} = 32$ *vs.* $N_{EC,s} = 40$ in Fig. 7). Consequently, it is concluded that operation with a slightly lower EC to PV cell ratio than the efficiency optimum (*i.e* at the TSP and to the left of the MPP in Fig. 2b) is desirable for directly coupled systems without DC-

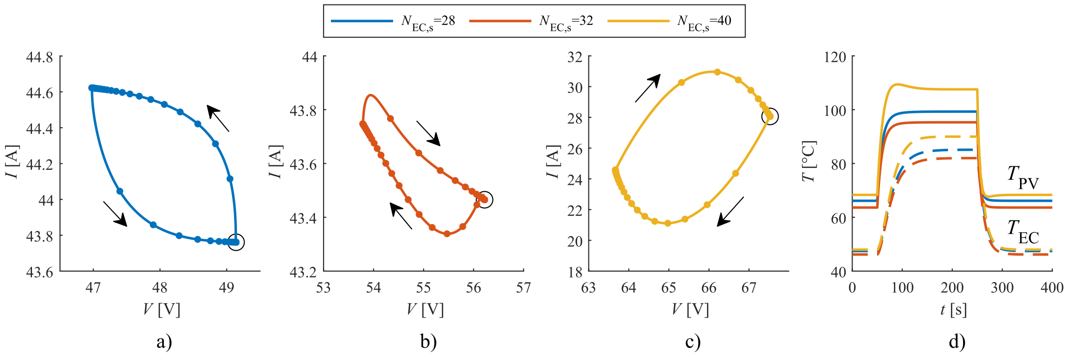

Fig. 5 – The trajectory of the operating point for varying $N_{EC,s}$ for a step change in F_{pump} (3 → 1 at 50 s and 1 → 3 L min^{-1} at 250 s) and DNI = 1000 W m^{-2} is shown in a), b) & c). Each marker is spaced at 5 s intervals and the arrows show direction of trajectory from the starting point (t = 0 s) denoted by a black circle. The corresponding PV and EC temperature changes are shown in d).

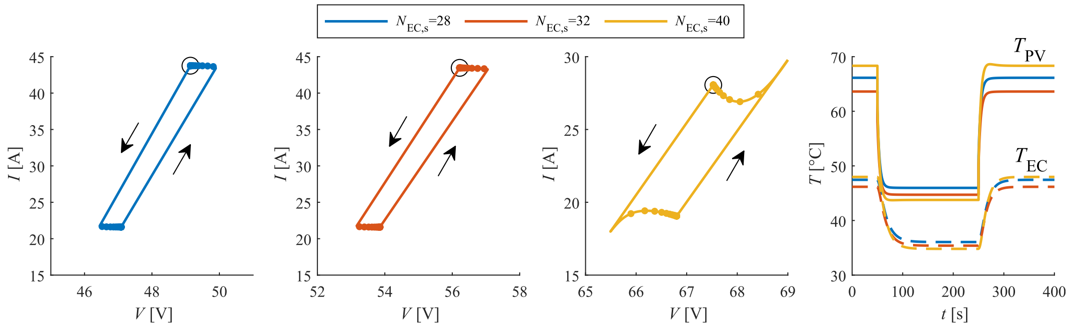

Fig. 6 – The trajectory of the operating point for varying $N_{EC,s}$ for a step change in DNI (1000 → 500 at 50 s and 500 → 1000 W m^{-2} at 250 s) and F_{pump} = 3 L min^{-1} is shown in a), b) & c). Each marker is spaced at 10 s intervals and the arrows show direction of trajectory from the starting point (t = 0 s) denoted by a black circle. The corresponding PV and EC temperature changes are shown in d).

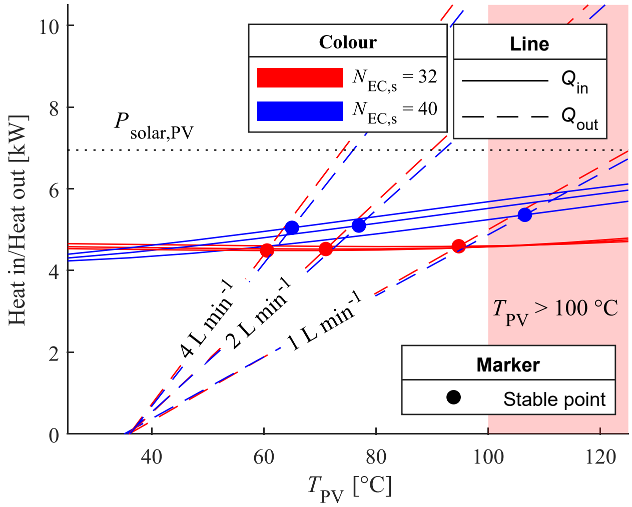

Fig. 7 – Semenov diagram of heat in and heat out of CPV module used to assess thermal stability of the operating points assuming DNI = 1000 W m^{-2}. Line style indicates directionality of heat in/out of PV, color indicates $N_{EC,s}$. The 6 intersection points, for F_{pump} of 1, 2, 4 L min^{-1} and $N_{EC,s}$ = 32 and 40 are shown as colored markers. (For interpretation of the references to color in this figure legend, the reader is referred Web version of this article.)

DC power conversion for both control and long term resilience to the life-time degradation in electrical performance. Furthermore, if the PV temperature range is less constrained by the risk of a drop in operating power causing the PV temperature to exceed a critical value (*i.e.* 100 °C), heat can be extracted at higher temperatures (*cf.* efficiency maximum in Fig. 3a for lower $N_{EC,s}$).

Opportunities for co-generation of heat and power

Given that a large fraction of the solar energy is converted to heat, integration with a process that requires heat will enable significant efficiency gains in a manner analogous to a PV-thermal collector or a combined heat and power plant. This concept has been previously experimentally demonstrated for similar systems, by Tembhurne et al. [8] (where there was a higher degree of thermal integration: PV and EC in monolithic stack where cooling water passes over front of solar cell) and by Tabanjat et al. [17] (where DC-DC power conversion was used and unconcentrated solar light was used with a single junction silicon PV module). In order to demonstrate the potential for waste heat utilisation of the integrated system, the maximum amount of thermal power that can be extracted above a given temperature is calculated. This corresponds to an ideal heat exchanger (effectiveness = 1).

The Sankey diagram, shown in Fig. 8 for example operating conditions, visualizes the transfer and conversion of power through the process whilst highlighting energetic losses. Significant energetic losses from the process are observed in the optics (*i.e.* absorbed, not intercepted and reflected at PV surface) and wasted heat (*i.e.* waste heat at low temperatures) whereas, whilst the PV performance is state-of-the-art, there is significant exergy destruction in the conversion of solar energy to electricity in the PV (*i.e.* 65.5% of the light is converted to heat). Furthermore, as the pumping power modeled here is small relative to the output fuel and heat powers (*e.g.* for 1.5 and 10 L min^{-1}, P_{pump} = ~0.35 and ~25 W respectively), the pumping power through the CPV and EC is neglected in Fig. 8 without introducing a significant error. However, it is important to note that accurate calculate of the pumping power is not the focus of this study and that the system pressure drop ($\Delta P \approx 0.1$ bar for the example shown in Fig. 8) will be a significant underestimate as the complete systems will comprise of multiple auxiliary component, such as heat exchangers, valves, gas separators *etc.*.

As the system temperature depends on operating conditions, notably water flowrate (in agreement with Ref. [8,17]), and the EC output temperature dictates the exergetic quality of the heat, low water flowrates will be required to extract the greatest amount of useful heat. This system efficiency η_{sys} dependence on flowrate can be seen in Fig. 9. This displays the significant co-generation system efficiency gains achievable assuming all heat above various temperatures (40, 50, 60, 70 °C) is utilized, for varying DNI conditions. Given that for $N_{EC,s}$ = 32 the intersection of the PV and EC curves in Fig. 2a lies to the left of the TSP, η_{H_2} remains comparatively constant

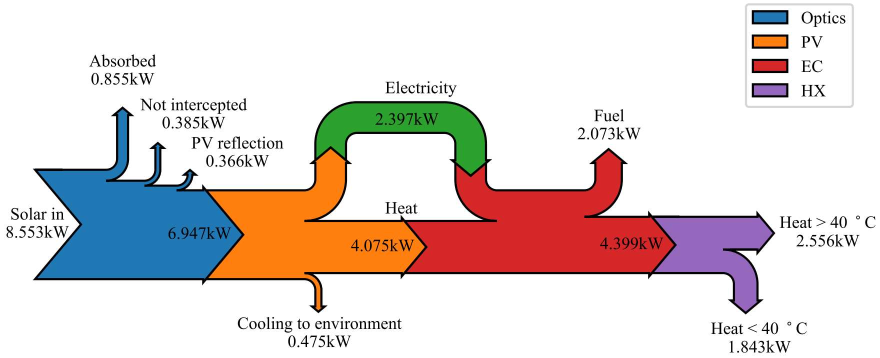

Fig. 8 – Sankey diagram of the solar-to-hydrogen & heat co-generation system for an example configuration and operating conditions (F_{pump} = 1.5 L min^{-1}, $N_{EC,s}$ = 32, DNI = 1000 W m^{-2}). Pumping power is not shown.

for all water flowrates in contrast to when the operating point is to the right of the TSP ($N_{EC,s}$ = 36, 38, 40 in Fig. 3a). This indicates that for a co-generation system which requires high operating temperatures to maximize thermal efficiency, it is necessary to match the PV to EC ratio accordingly to optimize η_{H_2} at maximum allowable temperature. According to Fig. 3a, this could impose a ~5% reduction in the optimum η_{H_2} for a specific $N_{EC,s}$ from ~21% to ~20%, but will permit lower flowrates and higher fluid outlet temperatures of up to ~70 °C, indicating the intrinsic compromise between maximising thermal power and hydrogen output. Furthermore, the water flowrate which optimizes the co-generation efficiency changes with DNI conditions, which suggests that water flowrate control would be an effective way to stabilize diurnal heat production.

Conclusions

A comprehensive dynamic model of a solar fuel processing system made of a thermally-integrated CPV-EC device utilizing a solar parabolic dish has been introduced. This included the mass, energy and momentum continuity equations for components critical to the coupled dynamic behavior *i.e.* PV, EC, pump, piping, and solar dish. Both electrical models for the PV and EC were temperature dependent and coupled to the respective thermal model. The behavior of an example implementation was then simulated using gPROMS, where the nominal H_2 production rate was ~2 kW and relevant model parameters were estimated or taken from literature.

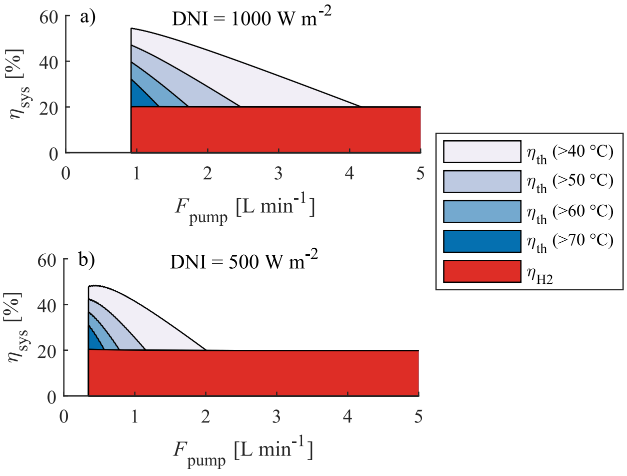

Fig. 9 – System efficiency of co-generation of fuel and heat *vs.* water flowrate for $N_{EC,s}$ = 32 and two values of DNI (500 and 1000 W m^{-2}) assuming all heat above specified temperature is useful.

A steady state analysis highlighted the impact of operating conditions and device configuration on the resulting system performance. In particular, contrasting behavior in response to temperature changes for varying numbers of series connected ECs was observed where either the temperature dependence of the short circuit current or the open circuit voltage would dominate the resulting performance. Solar-to-hydrogen system efficiencies in the range of 16–21% were predicted (with production rates of ~40 – 55g_{H_2} h^{-1} at DNI of 1000 W m^{-2}).

The system dynamic response was then simulated. This revealed that the behavior of the operating temperatures was mostly linear whereas for the electrical parameters of directly-coupled PV-EC, *i.e.* voltage and current, showed complex non-linear behavior. Upon closer inspection, the observed hysteresis in the electrical operating point was induced by the system thermal dynamics and, for the considered example system, the simulated dynamics are responsive enough (within 1–2 min) to envisage operating under challenging intermittent conditions.

Given the maximum operating temperature of the PV (T_{PV} < 100 °C), it is imperative to understand the negative effects of process deviations and the timescales at which a control system would have to respond. For both, pump failure and sudden electrical disconnection, changes to the control strategy should be implemented in seconds and therefore high frequency and reliable temperature monitoring is mandatory. Additionally, operating temperatures rapidly rise at lower flowrates (<2 L min^{-1}) and a temperature enhancing feedback mechanism was identified where an increase in the PV temperature causes a decrease in the operating point power leading to higher PV heat dissipation requirements. We demonstrated that, whilst undesirable, this phenomena does not behave like the classical thermal 'run-away' process as the temperature remains bounded assuming a reserve current inhibiting diode is installed. However, in order to ensure safe operation at high temperatures, the operating voltage should remain at lower voltages than the TSP voltage.

Finally, the potential for co-generation of the simultaneous heat and fuel generation was found to be very promising, where avenues for future research, such as the development of demand matching control strategies, were identified.

Declaration of competing interest

The authors declare that they have no known competing financial interests or personal relationships that could have appeared to influence the work reported in this paper.

Acknowledgements

This material is based upon work performed with the financial support of the Swiss Federal Office of Energy (grant #SI/501596–01) and a Starting Grant of the Swiss National Science Foundation (SCOUTS project, grant #155876). We thank Prof. François Maréchal (EPFL) for access to gPROMS.

Appendix A. Supplementary data

Supplementary data to this article can be found online at https://doi.org/10.1016/j.ijhydene.2020.12.151.

REFERENCES

[1] Jia J, Seitz LC, Benck JD, Huo Y, Chen Y, Ng JWD, Bilir T, Harris JS, Jaramillo TF. Solar water splitting by photovoltaic-electrolysis with a solar-to-hydrogen efficiency over 30%. Nat Commun 2016;7:13237. https://doi.org/10.1038/ncomms13237.

[2] Shaner MR, Atwater HA, Lewis NS, McFarland EW. A comparative technoeconomic analysis of renewable hydrogen production using solar energy. Energy Environ Sci 2016;9:2354–71. https://doi.org/10.1039/C5EE02573G.

[3] Schmidt O, Gambhir A, Staffell I, Hawkes A, Nelson J, Few S. Future cost and performance of water electrolysis: an expert elicitation study. Int J Hydrogen Energy 2017;42:30470–92. https://doi.org/10.1016/j.ijhydene.2017.10.045.

[4] Nemet GF. Beyond the learning curve: factors influencing cost reductions in photovoltaics. Energy Pol 2006;34:3218–32. https://doi.org/10.1016/j.enpol.2005.06.020.

[5] Philipps DS. Fraunhofer ise, W. Warmuth, PSE projects GmbH. Photovoltaics Report 2020:48.

[6] Glenk G, Reichelstein S. Economics of converting renewable power to hydrogen. Nature Energy 2019;4:216–22. https://doi.org/10.1038/s41560-019-0326-1.

[7] Tembhurne S, Haussener S. Integrated photo-electrochemical solar fuel generators under concentrated irradiation: I. 2-D non-isothermal multi-physics modeling. J Electrochem Soc 2016;163:H988–98. https://doi.org/10.1149/2.0311610jes.

[8] Tembhurne S, Nandjou F, Haussener S. A thermally synergistic photo-electrochemical hydrogen generator operating under concentrated solar irradiation. Nature Energy 2019;4:399–407. https://doi.org/10.1038/s41560-019-0373-7.

[9] Tembhurne S, Haussener S. Controlling strategies to maximize reliability of integrated photo-electrochemical devices exposed to realistic disturbances. Sustainable Energy & Fuels 2019;3:1297–306. https://doi.org/10.1039/C8SE00441B.

[10] Dumortier M, Tembhurne S, Haussener S. Holistic design guidelines for solar hydrogen production by photo-electrochemical routes. Energy Environ Sci 2015;8:3614–28. https://doi.org/10.1039/C5EE01821H.

[11] Briguglio N, Brunaccini G, Siracusano S, Randazzo N, Dispenza G, Ferraro M, Ornelas R, Aricò A, Antonucci V. Design and testing of a compact PEM electrolyzer system. Int J Hydrogen Energy 2013;38:11519–29. https://doi.org/10.1016/j.ijhydene.2013.04.091.

[12] García-Valverde R, Espinosa N, Urbina A. Optimized method for photovoltaic-water electrolyser direct coupling. Int J Hydrogen Energy 2011;36:10574–86. https://doi.org/10.1016/j.ijhydene.2011.05.179.

[13] Winkler MT, Cox CR, Nocera DG, Buonassisi T. Modeling integrated photovoltaic-electrochemical devices using steady-state equivalent circuits. Proc Natl Acad Sci Unit States Am 2013;110:E1076–82. https://doi.org/10.1073/pnas.1301532110.

[14] Sayedin F, Maroufmashat A, Roshandel R, Khavas SS. Optimal design and operation of a photovoltaic–electrolyser system using particle swarm optimisation. Int J Sustain Energy 2016;35:566–82. https://doi.org/10.1080/14786451.2014.922974.

[15] García-Valverde R, Miguel C, Martinezbejar R, Urbina A. Optimized photovoltaic generator–water electrolyser coupling through a controlled DC–DC converter. Int J Hydrogen Energy 2008;33:5352–62. https://doi.org/10.1016/j.ijhydene.2008.06.015.

[16] Özgirgin E, Devrim Y, Albostan A. Modeling and simulation of a hybrid photovoltaic (PV) module-electrolyzer-PEM fuel cell system for micro-cogeneration applications. Int J Hydrogen Energy 2015;40:15336–42. https://doi.org/10.1016/j.ijhydene.2015.06.122.

[17] Tabanjat A, Becherif M, Emziane M, Hissel D, Ramadan H, Mahmah B. Fuzzy logic-based water heating control methodology for the efficiency enhancement of hybrid PV–PEM electrolyser systems. Int J Hydrogen Energy 2015;40:2149–61. https://doi.org/10.1016/j.ijhydene.2014.11.135.

[18] Carmo M, Fritz DL, Mergel J, Stolten D. A comprehensive review on PEM water electrolysis. Int J Hydrogen Energy 2013;38:4901–34. https://doi.org/10.1016/j.ijhydene.2013.01.151.

[19] Gorgun H. Dynamic modelling of a proton exchange membrane (PEM) electrolyzer. Int J Hydrogen Energy 2006;31:29–38. https://doi.org/10.1016/j.ijhydene.2005.04.001.

[20] Awasthi A, Scott K, Basu S. Dynamic modeling and simulation of a proton exchange membrane electrolyzer for hydrogen production. Int J Hydrogen Energy 2011;36:14779–86. https://doi.org/10.1016/j.ijhydene.2011.03.045.

[21] García-Valverde R, Espinosa N, Urbina A. Simple PEM water electrolyser model and experimental validation. Int J Hydrogen Energy 2012;37:1927–38. https://doi.org/10.1016/j.ijhydene.2011.09.027.

[22] Lebbal M, Lecœuche S. Identification and monitoring of a PEM electrolyser based on dynamical modelling. Int J Hydrogen Energy 2009;34:5992–9. https://doi.org/10.1016/j.ijhydene.2009.02.003.

[23] Guilbert D, Vitale G. Dynamic emulation of a PEM electrolyzer by time constant based exponential model. Energies 2019;12:750. https://doi.org/10.3390/en12040750.

[24] Abdin Z, Webb C, Gray E. Modelling and simulation of a proton exchange membrane (PEM) electrolyser cell. Int J

Hydrogen Energy 2015;40:13243–57. https://doi.org/10.1016/j.ijhydene.2015.07.129.
- [25] Segev G, Mittelman G, Kribus A. Equivalent circuit models for triple-junction concentrator solar cells. Sol Energy Mater Sol Cell 2012;98:57–65. https://doi.org/10.1016/j.solmat.2011.10.013.
- [26] Sze SM, Ng KK. Physics of semiconductor devices. John Wiley & Sons; 2006.
- [27] G03 Committee. Tables for reference solar spectral irradiances: Direct normal and hemispherical on 37 tilted surface, technical report. ASTM International; 2012.
- [28] Singh P, Ravindra N. Temperature dependence of solar cell performance—an analysis. Sol Energy Mater Sol Cell 2012;101:36–45. https://doi.org/10.1016/j.solmat.2012.02.019.
- [29] Varshni YP. Temperature dependence of the energy gap in semiconductors. Physica 1967;34:149–54.
- [30] Vurgaftman I, Meyer JR, Ram-Mohan LR. Band parameters for III–V compound semiconductors and their alloys. J Appl Phys 2001;89:5815–75. https://doi.org/10.1063/1.1368156.
- [31] Royne A, Dey C, Mills D. Cooling of photovoltaic cells under concentrated illumination: a critical review. Sol Energy Mater Sol Cell 2005;86:451–83. https://doi.org/10.1016/j.solmat.2004.09.003.
- [32] Theristis M, O'Donovan TS. Electrical-thermal analysis of III–V triple-junction solar cells under variable spectra and ambient temperatures. Sol Energy 2015;118:533–46. https://doi.org/10.1016/j.solener.2015.06.003.
- [33] Duffie JA, Beckman WA. Solar engineering of thermal processes. 4th ed. ed. John Wiley & Sons, Inc; 2013.
- [34] Jakhar S, Soni M, Gakkhar N. Historical and recent development of concentrating photovoltaic cooling technologies. Renew Sustain Energy Rev 2016;60:41–59. https://doi.org/10.1016/j.rser.2016.01.083.
- [35] Muzychka YS, Yovanovich MM. Laminar forced convection heat transfer in the combined entry region of non-circular ducts. J Heat Tran 2004;126:54–61. https://doi.org/10.1115/1.1643752.
- [36] Incropera FP, Lavine AS, Bergman TL, DeWitt DP. Fundamentals of heat and mass transfer. Wiley; 2007.
- [37] Olivier P, Bourasseau C, Bouamama PB. Low-temperature electrolysis system modelling: a review. Renew Sustain Energy Rev 2017;78:280–300. https://doi.org/10.1016/j.rser.2017.03.099.
- [38] Olesen AC, Frensch SH, Kær SK. Towards uniformly distributed heat, mass and charge: a flow field design study for high pressure and high current density operation of PEM electrolysis cells. Electrochim Acta 2019;293:476–95. https://doi.org/10.1016/j.electacta.2018.10.008.
- [39] Linstrom PJ, Mallard W. NIST Chemistry webbook; NIST standard reference database No. 69. 2001.
- [40] Choi P. A simple model for solid polymer electrolyte (SPE) water electrolysis. Solid State Ionics 2004;175:535–9. https://doi.org/10.1016/j.ssi.2004.01.076.
- [41] Springer TE. Polymer electrolyte fuel cell model. J Electrochem Soc 1991;138:2334. https://doi.org/10.1149/1.2085971.
- [42] Schalenbach M, Carmo M, Fritz DL, Mergel J, Stolten D. Pressurized PEM water electrolysis: efficiency and gas crossover. Int J Hydrogen Energy 2013;38:14921–33. https://doi.org/10.1016/j.ijhydene.2013.09.013.
- [43] Coulson JM. Coulson & richardson's chemical engineering. Oxford: Butterworth-Heinemann; 1999.
- [44] Buscemi A, Lo Brano V, Chiaruzzi C, Ciulla G, Kalogeri C. A validated energy model of a solar dish-Stirling system considering the cleanliness of mirrors. Appl Energy 2020;260:114378. https://doi.org/10.1016/j.apenergy.2019.114378.
- [45] Process systems enterprise, gPROMS. 1997-2020. URL: www.psenterprise.com/gproms.
- [46] AZUR SPACE Solar Power GmbH. Datasheet - advanced dense array module 3C30M. 2016. URL: www.azurspace.com/images/pdfs/0003070-01-01_3C30M_ADAM.pdf.
- [47] Aiken DJ. High performance anti-reflection coatings for broadband multi-junction solar cells. Sol Energy Mater 2000:12.
- [48] Homier R, Jaouad A, Turala A, Valdivia CE, Masson D, Wallace SG, Fafard S, Ares R, Aimez V. Antireflection coating design for triple-junction III–V/Ge high-efficiency solar cells using low absorption PECVD silicon nitride. IEEE Journal of Photovoltaics 2012;2:393–7. https://doi.org/10.1109/JPHOTOV.2012.2198793.
- [49] Alam MS, Alouani AT. Dynamic modeling of photovoltaic module for real-time maximum power tracking. J Renew Sustain Energy 2010;2:043102. https://doi.org/10.1063/1.3435338.
- [50] Giner ELX, PEMI electrolyzer manual rev 1.0, [n.d].
- [51] Sheng W, Gasteiger HA, Shao-Horn Y. Hydrogen oxidation and evolution reaction kinetics on platinum: acid vs alkaline electrolytes. J Electrochem Soc 2010;157:B1529. https://doi.org/10.1149/1.3483106.
- [52] Siracusano S, Baglio V, Moukheiber E, Merlo L, Aricò A. Performance of a PEM water electrolyser combining an IrRu-oxide anode electrocatalyst and a short-side chain Aquivion membrane. Int J Hydrogen Energy 2015;40:14430–5. https://doi.org/10.1016/j.ijhydene.2015.04.159.
- [53] Siracusano S, Van Dijk N, Payne-Johnson E, Baglio V, Aricò A. Nanosized IrOx and IrRuOx electrocatalysts for the O2 evolution reaction in PEM water electrolysers. Appl Catal B Environ 2015;164:488–95. https://doi.org/10.1016/j.apcatb.2014.09.005.
- [54] Kadakia KS, Jampani PH, Velikokhatnyi OI, Datta MK, Park SK, Hong DH, Chung SJ, Kumta PN. Nanostructured F doped IrO2 electro-catalyst powders for PEM based water electrolysis. J Power Sources 2014;269:855–65. https://doi.org/10.1016/j.jpowsour.2014.07.045.
- [55] Suermann M, Schmidt TJ, Büchi FN. Comparing the kinetic activation energy of the oxygen evolution and reduction reactions. Electrochim Acta 2018;281:466–71. https://doi.org/10.1016/j.electacta.2018.05.150.
- [56] Durst J, Simon C, Hasché F, Gasteiger HA. Hydrogen oxidation and evolution reaction kinetics on carbon supported Pt, Ir, Rh, and Pd electrocatalysts in acidic media. J Electrochem Soc 2015;162:F190–203. https://doi.org/10.1149/2.0981501jes.
- [57] Ni M, Leung MK, Leung DY. Energy and exergy analysis of hydrogen production by a proton exchange membrane (PEM) electrolyzer plant. Energy Convers Manag 2008;49:2748–56. https://doi.org/10.1016/j.enconman.2008.03.018.
- [58] Heller PW, editor. The performance of concentrated solar power (CSP) systems: analysis, measurement and assessment. Cambridge, MA: Woodhead Publishing Series in Energy, Woodhead Publishing, an imprint of Elsevier; 2017.
- [59] Mancini T, Heller P, Butler B, Osborn B, Schiel W, Goldberg V, Buck R, Diver R, Andraka C, Moreno J. Dish-stirling systems: an overview of development and status. J Sol Energy Eng 2003;125:135–51. https://doi.org/10.1115/1.1562634.
- [60] Couper JR, Penney WR, Fair JR. Chemical process equipment-selection and design. 2nd ed. ed. Gulf Professional Publishing; 2009.
- [61] Kinsey GS, Hebert P, Barbour KE, Krut DD, Cotal HL, Sherif RA. Concentrator multijunction solar cell characteristics under variable intensity and temperature. Prog Photovoltaics Res Appl 2008;16:503–8. https://doi.org/10.1002/pip.834.

[62] Kinsey GS, Edmondson KM. Spectral response and energy output of concentrator multijunction solar cells. Prog Photovoltaics Res Appl 2009;17:279–88. https://doi.org/10.1002/pip.875.

[63] Lambkin JD, Considine L, Walsh S, O'Connor GM, McDonagh CJ, Glynn TJ. Temperature dependence of the photoluminescence intensity of ordered and disordered $In_{0.48}Ga_{0.52}P$. Appl Phys Lett 1994;65:73–5. https://doi.org/10.1063/1.113078.

[64] Fan JC. Theoretical temperature dependence of solar cell parameters. Sol Cell 1986;17:309–15. https://doi.org/10.1016/0379-6787(86)90020-7.

[65] Paul S, Roy JB, Basu PK. Empirical expressions for the alloy composition and temperature dependence of the band gap and intrinsic carrier density in $Ga_xIn_{1-x}As$. J Appl Phys 1991;69:827–9. https://doi.org/10.1063/1.348919.

[66] Ramires ML, Nieto de Castro CA, Nagasaka Y, Nagashima A, Assael MJ, Wakeham WA. Standard reference data for the thermal conductivity of water. J Phys Chem Ref Data 1995;24:1377–81.

[67] Pátek J, Hrubý J, Klomfar J, Součková M, Harvey AH. Reference correlations for thermophysical properties of liquid water at 0.1MPa. J Phys Chem Ref Data 2009;38:21–9. https://doi.org/10.1063/1.3043575.

[68] Lemmon EW, McLinden MO, Friend DG. Thermophysical properties of fluid systems. In: Linstrom P, Mallard W, editors. NIST chemistry WebBook, NIST standard reference database number 69. Gaithersburg MD: National Institute of Standards and Technology; 2018. 20899.

[69] Marangio F, Santarelli M, Cali M. Theoretical model and experimental analysis of a high pressure PEM water electrolyser for hydrogen production. Int J Hydrogen Energy 2009;34:1143–58. https://doi.org/10.1016/j.ijhydene.2008.11.083.

[70] Biaku C, Dale N, Mann M, Salehfar H, Peters A, Han T. A semiempirical study of the temperature dependence of the anode charge transfer coefficient of a 6kW PEM electrolyzer. Int J Hydrogen Energy 2008;33:4247–54. https://doi.org/10.1016/j.ijhydene.2008.06.006.

[71] Zawodzinski TA, Davey J, Valerio J, Gottesfeld S. The water content dependence of electro-osmotic drag in proton-conducting polymer electrolytes. Electrochim Acta 1995;40:297–302. https://doi.org/10.1016/0013-4686(94)00277-8.